Advanced Materials Technologies

ADVANCED MATERIALS TECHNOLOGIES
www.advmattechnol.com

RESEARCH ARTICLE OPEN ACCESS

Solid Particle-Liquid Metal Mixtures for Robust High-Current Interconnects in Stretchable Electronics and Soft Robotics

Ethan J. Krings[1] | Calan Brant[1] | Carson Emeigh[2] | Donovan Vincent Jr.[3,4] | Ravi Tutika[1] | Sangjin Ryu[5] | Eric J. Markvicka[1,6,7]

[1]Smart Materials and Robotics Laboratory, Department of Mechanical & Materials Engineering, College of Engineering, University of Nebraska–Lincoln, Lincoln, Nebraska, USA | [2]Department of Mechanical & Materials Engineering, University of Nebraska–Lincoln, Lincoln, Nebraska, USA | [3]Department of Chemical and Biomolecular Engineering, Johns Hopkins University, Baltimore, Maryland, USA | [4]Chemical Engineering, Manhattan University, New York City, New York, USA | [5]Department of Mechanical Engineering, Bradley University, Peoria, Illinois, USA | [6]Department of Electrical & Computer Engineering, University of Nebraska–Lincoln, Lincoln, Nebraska, USA | [7]School of Computing, University of Nebraska–Lincoln, Lincoln, Nebraska, USA

Correspondence: Eric J. Markvicka (eric.markvicka@unl.edu)

Received: 10 April 2026 | **Revised:** 6 May 2026 | **Accepted:** 13 May 2026

Keywords: electromigration | high current density | liquid metals | stretchable electronics | thermal failure

ABSTRACT

Electromigration and thermal degradation limit the reliability of interconnects in stretchable electronics and soft robotics, particularly in room-temperature liquid metals (LMs), where weaker interatomic bonds accelerate failure at lower current densities. To address this, we created solid particle-LM mixtures that incorporate metallic (iron and tungsten) and non-metallic (glass) particle fillers, which suppress electromigration and thermal degradation. These LM mixtures are able to achieve a maximum current density exceeding 2.5×10^8 A·m^{-2} (80% improvement over unfilled LM) while extending operational lifetimes by $>124,000\times$ under a constant DC current density of 1.1×10^8 A·m^{-2}. Despite a small decrease in electrical conductivity at higher filler loadings, the LM mixtures retained their fluidic properties, which are critical for integration in soft matter systems. Furthermore, the low particle loading (5 vol.%) enhanced Joule heating performance, enabling electrothermal actuators to achieve faster actuation speeds and higher cyclic frequencies compared to their pure LM counterparts. By increasing the electrical stability through solid particle fillers, this facile strategy offers a scalable pathway toward robust, high-current LM interconnects for next-generation stretchable electronics and soft robotic systems.

1 | Introduction

High-current stretchable electronics are critical for powering Joule heating elements [1–3], electromagnetic actuators [4–6], and wireless power transfer [7–9]. However, stretchable interconnects, such as Gallium-based liquid metal (LM) alloys [10–12], face a fundamental reliability challenge under sustained electrical loading. LM alloys undergo failure driven by electromigration and thermal failure mechanisms [13–16], a process that is accelerated in liquid interconnects. Nevertheless, LMs are widely used in wearable electronics and soft robotics with moderate electrical loads owing to their favorable combination of low viscosity with high electrical and thermal conductivity [17–27]. However, under high current densities, their liquid nature promotes void formation, localized heating, and rapid progression to open-circuit failure, typically within seconds to minutes. This failure mechanism contrasts with solid-metal interconnects and restricts the use of LM conductors in high-power applications.

https://doi.org/10.1002/admt.71060

Electromigration is a well-studied phenomenon in thin-metal conductors used in integrated circuits, defined as the net displacement of metal ions within a conductor due to an applied current, which can lead to open-circuit failure [28]. This process occurs in both solid and liquid conductors. However, LMs typically experience electromigration and thermal failure at lower current densities and shorter timescales due to weaker interatomic forces [29–34]. Unlike solid conductors, where electron wind force primarily causes ion motion, electromigration in many LMs is dominated by electrostatic forces. These forces lead to void formation at the anode and hillock growth at the cathode. To address electromigration and thermal failure in Ga-based LM circuits, several mitigation strategies have been introduced, including the use of alternating current [15], reinforcing LM conductors with carbon nanotubes [16], modifying the substrate surface [35, 36], and integrated cooling systems [14]. While these approaches have improved the median lifetime and maximum current densities of LM conductors by modifying the thermal or rheological properties of the LM conductor or environment, they remain constrained by limits of the applied current (≤ 100 mA), material viscosity, scalability, and overall cost. Moreover, AC current-based techniques and active interconnect cooling strategies are challenging to implement in conventional direct current (DC) circuit architectures and untethered applications. A promising alternative strategy to enhance the thermo-mechanical properties, rheology, and consistency of LM conductors is the incorporation of solid particle fillers [25, 37–43]. Previous studies have investigated a variety of biphasic LM-particle composites, including the addition of magnetic fillers such as iron (Fe) and insulating particles like glass beads to tune the thermal, electrical, and mechanical response of the resulting mixture [23, 44–47]. However, the impact of these particle additions on electromigration and thermal failure mechanisms in LM systems is not yet fully understood.

Here, we demonstrate that dispersing solid microparticles within LMs disrupts electromigration pathways while preserving their fluidic characteristics. This strategy aligns with broader interface engineering principles used in high-performance functional materials to enhance reliability under extreme operational stresses [48–52]. The proposed electromigration phenomenon is analogous to thermally triggered muscle contraction where externally supplied energy biases microscopic thermal motion within an asymmetric protein network. This process enables directed mass transport that consequently produces macroscopic effects (Figure 1a). The distribution of the solid particles, which is largely determined by their density relative to the LM, plays a critical role in the performance and reliability of LM interconnects. Fillers with densities similar to LM, such as iron (Fe), achieve uniform dispersion and facilitate stable flow dynamics within the mixture. This stability, combined with the fillers' ability to support the growth of a protective Ga-oxide shell at elevated temperatures, significantly extends interconnect lifespan by delaying failure. As the solid metallic particle volume loading in LM increases, the failure mechanism of the interconnects shifts from electromigration, characterized by the formation of voids and hillocks, to thermal failure at temperatures exceeding 500°C (Figure 1b). Specifically, the metallic fillers disrupt the flow of metal ions within the LM mixture, mitigating electromigration induced failure at low current densities ($< 1.5 \times 10^8$ A·m^{-2}), a regime where pure LM typically fails. The LM mixtures are able to achieve higher current densities and temperatures to support the growth of a protective Ga oxide shell, which prevents the formation of voids and hillocks and stabilizes the electrical conductor at high current density conditions ($> 1.5 \times 10^8$ A·m^{-2}). Furthermore, as shown in Figure 1c, solid particle-LM mixtures are able to achieve a significant increase in maximum current density exceeding 2.5×10^8 A·m^{-2}, an 80% improvement over unfilled LMs, while extending the operational lifetime by $> 124,000\times$ under a constant DC current density (1.1×10^8 A·m^{-2}). While this multi-filler strategy offers a robust solution for high-power applications, it introduces inherent trade-offs common to composite design, such as the potential for filler sedimentation and a minor reduction in bulk conductivity compared to pure LM. Nevertheless, the enhanced resilience enables high-performance Joule heaters with faster actuation speeds and increased cyclic frequency. Solid particle additives, even at low volume loadings, offer a promising solution to extend the lifetime of LM conductors while significantly increasing current density for high-power applications. These advancements ultimately provide the structural and electrical reliability necessary to support the miniaturization of stretchable electronics and soft robotic systems.

2 | Results and Discussion

2.1 | Fabrication Methodology

Solid particle-LM mixtures were created with a wide range of solid particle additives in terms of their metallic conductivity and density (ρ). Specifically, we selected iron (Fe), tungsten (W), and glass. Fe ($\rho_{Fe} = 7.9$ g·cm^{-3}) and W ($\rho_W = 19.3$ g·cm^{-3}) are metallic particles with densities similar and $> 3\times\rho_{LM}$, respectively. Lastly, hollow glass microspheres ($\rho = 1.1$ g·cm^{-3}) were selected as a low-density, non-metallic filler to understand the effects of nonconducting solid fillers on electromigration. All the particles had a mean diameter on the order of 10 μm to reduce agglomeration and air entrapment during mixing [53, 54] and to prevent the formation of irregular cross-sections when creating the LM interconnects. Particles with different densities were chosen to study if mass and distribution of particles played a role in restricting LM flow caused by electrostatic forces during electromigration.

Eutectic gallium–indium (EGaIn) was selected as the LM due to its low viscosity, low toxicity, and high electrical and thermal conductivity [55]. The solid particles were dispersed in LM by shear mixing under ambient conditions to create a stable suspension (Figure S1) [37]. Particle volume fractions of $\phi = 0.01$, 0.05, and 0.10 were considered for each particle and compared with pure LM ($\phi = 0$). To determine the effects of the solid particle additives on the failure mechanisms, dogbone-shaped conductors were created. The samples were created by first spraying a thin adhesion layer (< 20 μm) of LM onto a high-temperature quartz slide. The solid particle-LM mixture was then blade-coated onto the pattern (Figure S2a–d). The dogbone shape, shown in Figure 2a, was designed to fail in a 2 mm × 1 mm × 0.14 mm volume in the center of the sample as the applied electrical current increased. Before testing, laser profilometry (VK-X200K; Keyence) was used to measure the

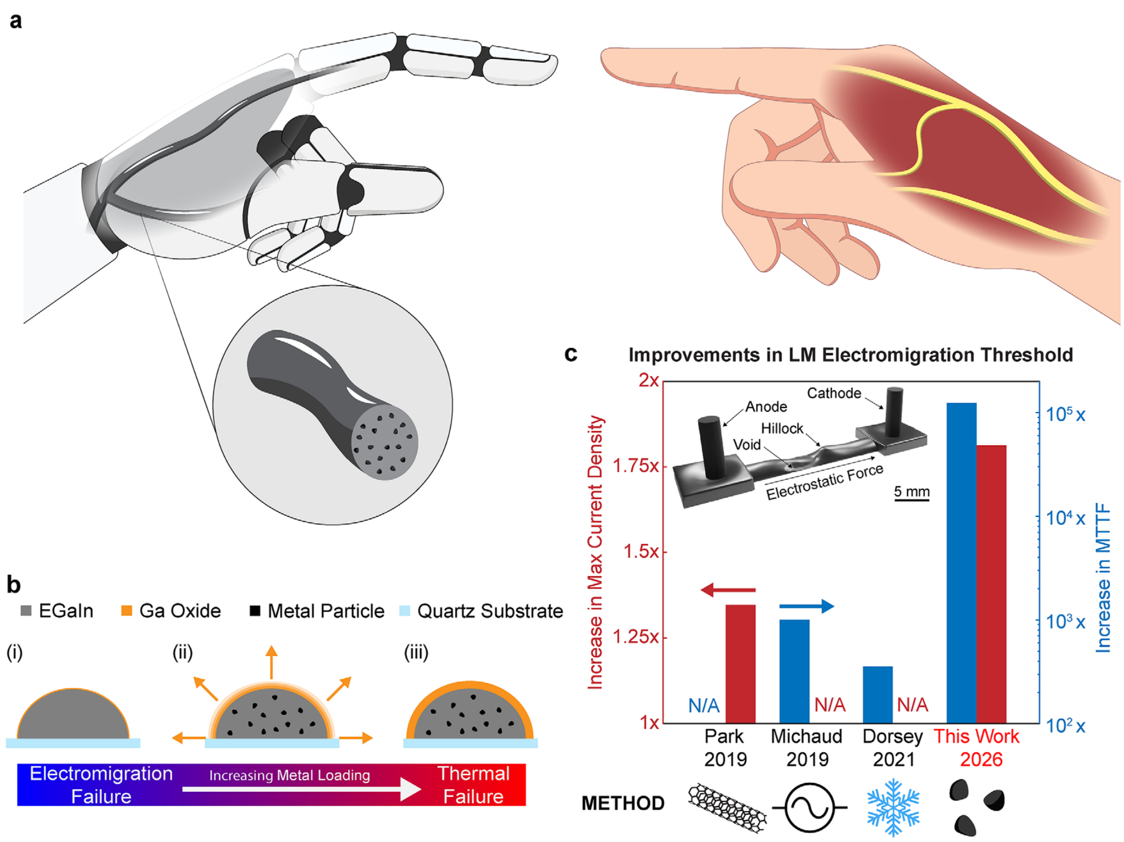

FIGURE 1 | Solid particle-LM mixtures for high current applications. (a) Conceptualization of solid particle-LM interconnects (inset) embedded into soft robotic actuators. The thermal stimulus provided by the LM interconnects is similar to nerves stimulating muscle contraction. (b) As the loading of the metal particles is increased, the failure mode transitions from electromigration to thermal failure, extending the lifetime and maximum current density of the LM interconnects due to the LM oxide shell growth. (c) Improvements in maximum current density and mean time to failure (MTTF) in our solid–liquid LM mixtures compared to other mitigation strategies.

average cross-sectional area of the center of the dogbone sample, which was used to calculate the current density.

2.2 | Electrical Properties of Solid Particle-LM Mixtures

The dogbone samples were electrically interfaced using W electrodes, as W is resistant to gallium corrosion [37]. The W probes were placed on the contact pads of the dogbone and connected to a DC power supply in constant current mode. A current of 0.5 A was applied across the dogbone sample and the sourced voltage was measured. To determine the maximum current density, the current was increased in 0.5 A increments and held for 30 s intervals until the sample failed. Failure was defined by a fixed threshold of 10 V, representing the point of catastrophic electrical breakdown. As initial sample resistances varied with filler loading, this 10 V limit corresponded to a 2× to 10× increase over the baseline measured voltage across the dogbone samples. The maximum current density at failure for each sample was calculated by dividing the applied current at failure by the measured cross-sectional area of the sample.

A photograph, laser profile scan, and the corresponding trace height map for both pure LM ($\phi = 0$) and an LM-Fe mixture ($\phi = 0.05$) before and after electrical failure is shown in Figure 2a,b, respectively. As shown in Figure 2a, before testing (blue line), the anode side of the pure LM dogbone had excess material. Following electrical failure (red line), material migration from the anode to the cathode side was observed, which is consistent with previous studies [29]. Minimal material migration was observed for the LM-Fe mixture shown in Figure 2b. In addition, the surface of the LM-Fe mixture changed from a highly reflective silver to a dull reddish-brown color, indicating the growth of the Ga oxide shell. White smoke was also observed during failure, with remnants visible around the location of failure (Figure 2b, inset). High-speed video (Movie S1) was used to capture the rapid sequence of events leading to failure, highlighting the abrupt nature of the breakdown, which occurs within a 0.23-s interval. Selected frames from this sequence are shown in Figure 2c,d.

The maximum and normalized current density for the LM mixtures is shown in Figure S3a and Figure 2e, respectively. The unfilled LM had a maximum current density of $1.08 \pm 0.17 \times 10^8$ A·m^{-2}. We first considered LM mixtures with glass microspheres, a low-density, non-conductive filler. At volume loadings of $\phi = 0.01$ and 0.05, the current density at failure was reduced by 10% and 17%, respectively (Figure 2e). This reduction could be attributed to the non-conductive glass spheres effectively reducing the cross-sectional area of the LM trace. However, at a higher loading of glass microspheres ($\phi = 0.10$), the maximum current density increased by 12% compared to the unfilled sample.

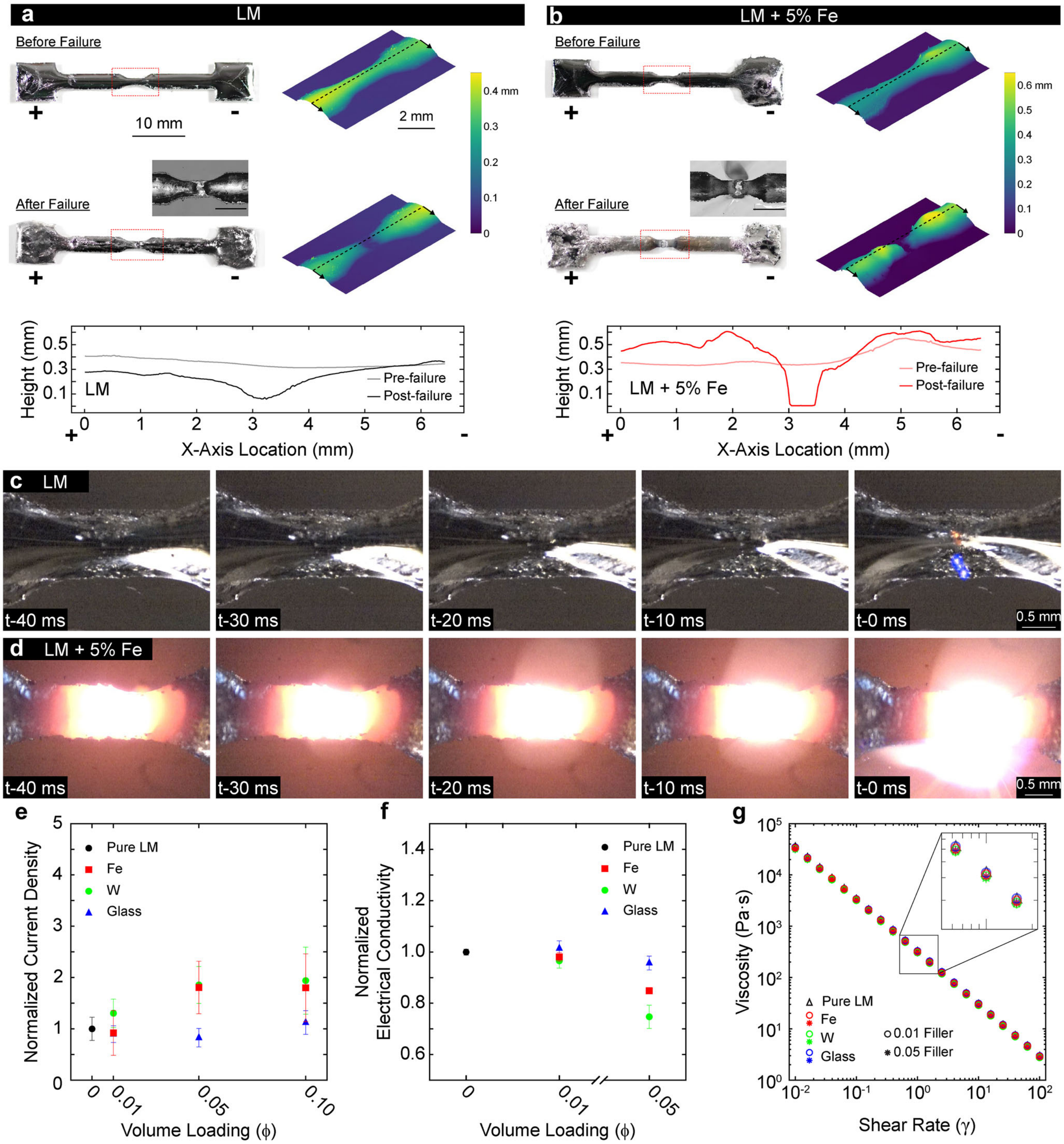

FIGURE 2 | Properties of the solid particle-LM mixtures. (a–b) Photographs, laser profile scans, and trace cross sections of pure LM and $\phi = 0.05$ Fe mixture before and after electrical failure. Inset scale bar 2 mm. Plus and minus signs indicate anode and cathode. Laser profile scans and cross section trace of the LM samples before and after failure. (c) Close-up of EGaIn dogbone sample from 40 ms before failure until circuit failure due to electromigration. (d) Close-up of $\phi = 0.05$ Fe dogbone sample from 40 ms before failure until circuit failure due to thermal failure. (e) Maximum achieved current density for LM mixtures with Fe, W, and Glass particle fillers at particle volume loadings of $\phi = 0.01$, 0.05, and 0.10 normalized by unfilled LM ($n = 5$). (f) Effect of particle loading and type on electrical conductivity of solid particle-LM mixtures ($n = 3$). Electrical conductivity is normalized by unfilled LM. g) Effect of particle loading and type on viscosity of solid particle-LM mixtures ($n = 3$). (e–g) All error bars represent ±1 SD and are not displayed if smaller than the data point size.

Next, we investigated two metallic fillers, Fe and W, which do not form intermetallic species when mixed with Ga-based LMs. Fe has a high thermal and electrical conductivity with a density similar to LM ($7.9\ \mathrm{g \cdot cm^{-3}}$), while W also has a high thermal and electrical conductivity but density $> 3\times$ that of LM ($19.3\ \mathrm{g \cdot Cm^{-3}}$). For LM-Fe mixtures, at a volume loading of $\phi = 0.01$, the maximum current density was 8% lower than unfilled LM. However, at $\phi = 0.05$, the maximum current density was 81% higher. Increasing the volume loading to $\phi = 0.10$ did not result in a significant increase in maximum current density compared to $\phi = 0.05$. For LM-W mixtures, the maximum current density increased by 30% compared to LM at $\phi = 0.01$. Similar to the LM-Fe mixtures, a significant increase in maximum current density was observed when the volume loading was increased to $\phi = 0.05$, while the maximum current density between $\phi = 0.05$ and $\phi = 0.10$ remained relatively unchanged. The voltage versus current density curves for all LM-W, Fe, and glass testing conditions are shown in Figure S4.

These findings reveal a non-linear relationship between filler volume loading and maximum current density for both Fe and W. The most significant improvements were observed at moderate volume loadings ($\phi = 0.05$) for both metallic fillers, with no significant improvements at higher loadings. This plateau is likely related to the observed failure modes. At low loadings ($\phi \le 0.01$) failure was primarily driven by electromigration, as shown by the displacement of LM in the laser profiles (Figure 2a). In contrast, at higher loadings ($\phi = 0.05$ and 0.10), the samples exhibited significant surface changes, from a reflective silver to a dull reddish-brown, along with visible white smoke and residue at failure (Figure 2b), indicating a shift in the failure mechanism. From these observations, we believe the higher loading ($\phi \ge 0.05$) samples failed due to a combination of electromigration and excessive Joule heating, as supported by the appearance of a white incandescent glow (suggesting temperatures above 1,300°C; Figure S2e) and pitting in the underlying quartz glass slides, which melts above 1,700°C (Figure S5b,c). Notably, when glass microspheres were used as fillers, only minimal changes in maximum current density were observed across all loadings, underscoring the unique impact of metallic fillers on both performance and failure mechanisms.

To understand other possible mechanisms influencing the failure behavior of the LM mixtures, we investigated the electrical conductivity as a function of particle type and loading, which is known to play an important role in electromigration failure [36]. The conductivity of the unfilled LM was $\sigma = 3.42 \times 10^4\ \mathrm{S \cdot cm^{-1}}$ (Figure S3), which is in agreement with previous values reported in literature [56, 57]. The addition of glass microspheres had little impact on the electrical conductivity, with only a slight increase of 1.4% and a decrease of 4% at volume loadings of $\phi = 0.01$ and 0.05, respectively (Figure 2f). A decrease in electrical conductivity was also observed for Fe fillers as well. A modest 2% decrease in conductivity was observed for $\phi = 0.01$, while a larger 15% decrease was recorded for $\phi = 0.05$. W fillers caused the most significant decrease in conductivity as the volume loading increased. A modest 3.5% decrease in conductivity was observed for $\phi = 0.01$, while a substantial 25% decrease was recorded for $\phi = 0.05$.

These observations reveal a complex and counterintuitive relationship between particle type, filler loading, and electrical conductivity in solid particle-LM mixtures. We expected that metallic fillers, W and Fe, would have caused the smallest change in electrical conductivity compared to glass. However, the opposite trend was observed. The process of incorporating non-alloying particles into LM involves an oxide-assisted mechanism, where Ga oxide flakes adhere to the particles, promoting LM wetting and facilitating their incorporation into the LM (Figure S6) [37]. During mixing, air voids, due to agglomeration of Ga oxide flakes, are inevitably introduced into the LM [58, 59], as observed by the measured density being lower than the theoretical prediction (Figure S7). Longer mixing times were required when creating the W and Fe mixtures with LM, leading to increased void formation and air entrapment. Further, the presence of an oxide layer on the sourced W and Fe metallic particles add to higher interfacial resistance at the LM-solid particle interface. As a result, LM mixtures with glass fillers exhibited smaller decreases in electrical conductivity compared to those with W and Fe fillers, highlighting the critical influence of processing conditions on the electrical properties of LM mixtures.

2.3 | Rheological Properties of Solid Particle-LM Mixtures

The effects of filler type (glass, Fe, and W) on the viscosity of the solid particle-LM mixtures was examined for volume loadings of $\phi = 0$, 0.01, and 0.05. The viscosity of unfilled LM ($\phi = 0$) decreased as the shear rate increased and exhibited a shear thinning behavior, which could be represented by the power function $\mu = 315.85\dot{\gamma}^{-1.02}$. The viscosity of the LM mixtures ranged from 3 to $3 \times 10^4\ \mathrm{Pa \cdot s}$, and displayed shear thinning behavior for all combinations of volume loading and filler type (Figure 2g). Notably, the viscosity of the LM mixtures remained similar to the viscosity of the unfilled LM, indicating that the effect of the fillers was negligible for all combinations of filler type and volume loading. This negligible change in viscosity may be attributed to the presence of an oxide layer on the side surface of the LM samples that is exposed to ambient air, which is known to increase viscosity [10]. In addition, the negligible impact of the fillers could be related to the low volume loadings investigated. Our previous study showed that increasing the volume loading of glass microspheres above 30% significantly increased the viscosity of the LM mixtures, which transitioned from a liquid to paste-like consistency [23].

2.4 | Effects of Gallium Oxide on Electrical Failure

The effects of Ga oxide on electrical failure in LM systems are multifaceted and highly dependent on both processing and operational conditions. The process of incorporating non-alloying particles into LM is strongly influenced by the wetting behavior of the particles, which dictates the required mixing time and, consequently, the amount of Ga oxide introduced into the LM [37, 58, 59]. To assess the influence of the Ga oxide content on LM electrical failure, Ga oxide was introduced into pure LM using an overhead mixer (Figure S6, with shear mixing times of 1 to 5 min. As shown in Figure S8, increasing the mixing time and therefore

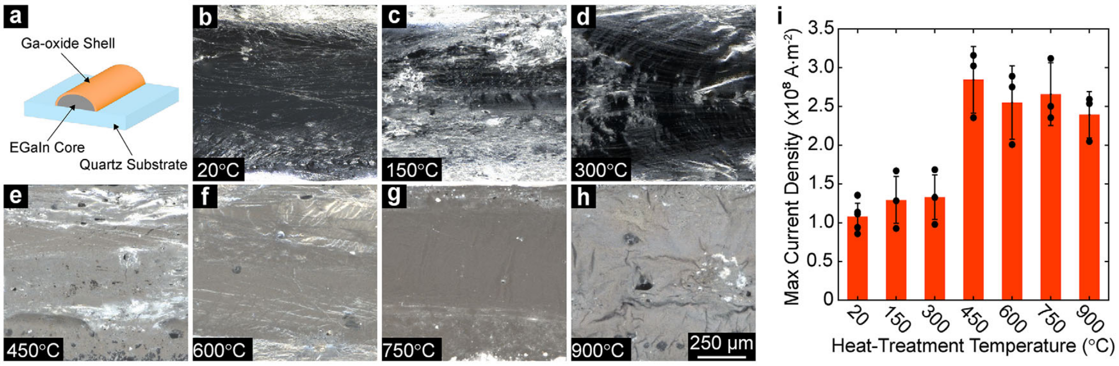

FIGURE 3 | Oxide shell growth due to heat treatment. (a) Schematic of oxide shell growth on surface of EGaIn trace due to high temperature heat treatment. (b–h) optical micrographs of oxidized EGaIn trace surface from 20 to 900°C. (i) Maximum current density of dogbone samples heat-treated at different temperatures ($n = 3$). All error bars represent ±1 SD and are not displayed if smaller than the data point size.

the oxide content led to a decrease in the maximum current density, even as the consistency of LM transitioned from liquid to paste-like. The significant decrease in the maximum current density is attributed to the increased presence of air voids, which expand at elevated temperatures and accelerate electromigration and thermal failure.

The ability of LM mixtures to sustain high current densities and reach elevated temperatures can lead to the thickening of the Ga oxide shell (Figure 3a), a process that occurs at temperatures above 400°C [18, 60, 61]. To investigate the effects of temperature and Ga oxide shell growth on LM electrical failure, dogbone samples without fillers ($\phi = 0$) were heat-treated for 30 min at temperatures ranging from 150 to 900°C in increments of 150°C. A visible change in the surface appearance was observed for samples treated at 450°C or higher, transitioning from a silvery and highly reflective finish to a dull grayish-brown color (Figure 3b–h). This color change is associated with temperature-driven oxidation of the LM oxide shell [61]. Notably, this observation of temperature-driven oxidation corresponds with an increase in the maximum current density from less than 1.51.5 × 10^8 A·m^{-2} to greater than 2.52.5 × 10^8 A·m^{-2} (Figure 3i). These results indicate that the thickened oxide shell serves as a protective coating that suppresses the formation of void and hillock failure morphologies, which are observed in samples heat-treated at lower temperatures (Figure 2a,b). A similar mechanism has been shown to delay electromigration failure in copper interconnects using a hexagonal boron nitride monolayer [62].

When considering the increase in maximum current density that is observed for LM mixtures that have not been heat-treated, the solid particle fillers within the LM create discontinuities in the current density distribution. This phenomenon, known as current crowding, forces current lines to compress in the narrow LM channels between solid fillers. This localized increase in current density facilitates localized heating >400 °C, and promotes the growth of a protective Ga oxide shell. This growth is further supported by the fillers acting as heterogeneous nucleation sites and mechanical anchors that stabilize the fragile oxide skin against thermal expansion. Additionally, the electrochemical potential difference between the metallic fillers and the gallium can facilitate localized oxidation at the interfaces, resulting in a more robust and continuous protective layer. Although the liquid nature of the interconnects makes cross-sectional SEM analysis of failed samples challenging without specialized cryo-stabilization, the morphological evidence of suppressed electromigration failure represents the protective behavior observed in our controlled heat-treatment experiments. This thickened Ga oxide shell effectively bridges the gap between low-temperature electromigration failure and high-temperature thermal failure, highlighting that relatively small particle loadings ($\phi = 0.05$) can significantly improve the maximum current density of LM-based interconnects as compared to unfilled LM evaluated at the same conditions (Figure 1c).

2.5 | Time to Failure Analysis

Time-to-failure experiments are essential to quantify the lifetime and assess the reliability of LM interconnects with different particle fillers as electromigration is a time-dependent degradation process. Such tests are usually performed in an accelerated manner at elevated current density or temperature, rather than normal operating conditions, for practical evaluation of the failure behavior. Here, we applied a constant current across the dogbone sample until the voltage exceeded 10 V, indicating electrical failure. A current density of 1.1 × 10^8 A·m^{-2} was selected because it caused an instantaneous failure in the unfilled LM interconnects ($\phi = 0$), while still allowing interconnects with LM mixtures to fail within a practical time frame. The cross-sectional area of each dogbone sample was measured using a laser profilometer and the required current to achieve the target current density was calculated. To prevent premature failure from inrush current, a controlled current ramp of 1 A · s^{-1} was applied at the start of each test until the desired current was reached. Samples that failed during this initial ramp phase were recorded as having a failure time of 1 millisecond.

The lifetimes of the LM traces were compared using Kaplan-Meier curves (Figure 4a) and a scatter plot (Figure 4b) over 3.6 weeks. All unfilled LM samples failed within the first 2.5 s, which is consistent with previous maximum current density tests, with 80% of the samples failing within 25 milliseconds. The LM mixtures containing glass microspheres performed similar to the unfilled LM and were the only mixtures where the time to failure decreased with increasing particle loading. The $\phi = 0.01$ glass

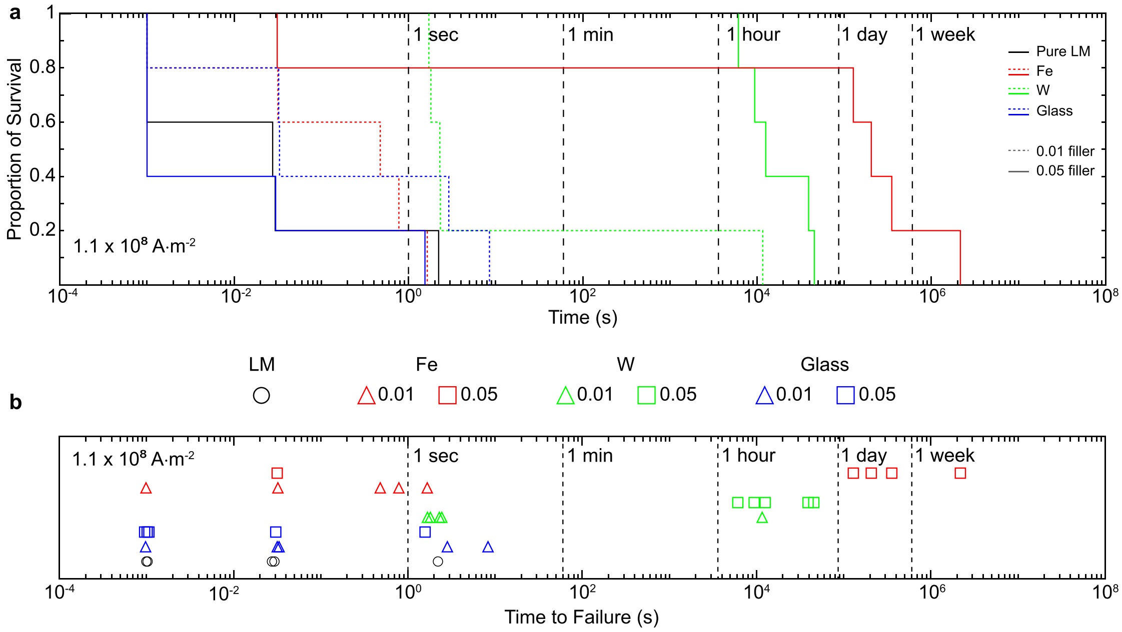

FIGURE 4 | Behavior and lifetime of solid particle-LM mixtures over 3.6 weeks. (a) Proportion of survival, and (b) Timeline showing failure of unfilled LM and solid particle-LM mixtures with an applied current density of 1.1×10^8 A·m^{-2} ($n = 5$).

microsphere samples were observed to slightly out-perform the unfilled LM samples, with a majority failing before 1 s and the longest sample surviving just over 8 s. In contrast, more than half of the $\phi = 0.05$ glass microsphere samples failed during the ramp-up phase, and the longest-lasting sample failed at 1.5 s. Similarly, $\phi = 0.01$ Fe samples failed nearly instantaneously, with the longest surviving sample lasting just 1.6 s. Notably, the $\phi = 0.05$ Fe samples had the longest lifespan of all the mixtures, with 80% of the samples surviving for over one day, and the longest sample lasting for approximately 25 days. This marks a six order of magnitude increase in survival time compared to the longest-lasting unfilled LM sample. The W samples with $\phi = 0.01$ showed a similar behavior to other $\phi = 0.01$ samples, with most failing before 2.5 s. However, the longest-lasting sample failed around 3 h. Increasing the volume loading of W up to $\phi = 0.05$ increased the survivability of the LM traces, with all samples failing between 1.7 and 12.6 h, a nearly five order of magnitude increase as compared to the unfilled LM sample. A timeline illustrating the time-to-failure for all tested samples is shown in Figure 4b.

The increased lifetime of LM mixtures with Fe and W particles ($\phi = 0.05$) can be attributed to the higher sample temperatures that were achieved during testing ($>400°$C), which led to the thickening of the oxide layer. Similar to the maximum current density experiments, this thickened Ga oxide shell served as a protective layer that suppressed the formation of void and hillock failure morphologies. At elevated temperatures, the oxide shell continued to grow until it eventually fractured under thermally induced stresses [61]. This thermomechanical fracture likely coincided with electromigration failure of the LM interconnect. However, we were unable to directly observe this process due to the abrupt and catastrophic nature of the failure as shown in Figure 2b,d and Movie S1.

The difference in lifespan between the LM-Fe and LM-W mixtures ($\phi = 0.05$) is likely attributed to the difference in filler density. Tungsten, with the highest density ($\rho_W = 19.3\ \mathrm{g \cdot cm^{-3}}$; $>3{\times}\rho_{LM}$), tends to settle in the LM, leading to a nonuniform dispersion. This settling behavior can be substantiated by Stokes' Law, which defines the terminal settling velocity (v_t) as proportional to the density difference between the particle and the fluid ($2(\rho_p - \rho_f)gR^2/9\mu$). For a 10 µm particle in EGaIn ($\mu \approx 2$ mPa · s) [63, 64], the calculated v_t for W is approximately 35.5 µm · s^{-1}. In an interconnect with a thickness of ≈0.15 mm, W particles would traverse the entire channel in only 4.2 s, leading to rapid sedimentation during the 30 s experimental hold intervals. This segregation results in localized regions of reduced current density, resulting in LM-W interconnects with shorter lifespans. In contrast, Fe particles ($\rho_{Fe} = 7.9\ \mathrm{g \cdot cm^{-3}}$), have a density closer to that of LM, allowing the particles to remain more uniformly dispersed. With a significantly lower calculated settling velocity ($v_t \approx 4.4$ µm · s^{-1}), Fe particles remain distributed within the liquid metal matrix for the duration of the experimental cycles. This uniformity causes current crowding effects to overlap and interact, creating a more complex current density distribution, which provides greater resistance to electromigration failure.

2.6 | LM Joule Heater for Soft Electrothermal Actuators

Soft electrothermal actuators are a promising alternative to non-electrical methods like pneumatics for untethered systems, as they do not require bulky auxiliary equipment [65, 66]. Such actuators can be created by incorporating resistive Joule heating elements into shape memory polymers, such as liquid crystal elastomers (LCEs), which undergo shape change upon thermal activation [2, 13, 67, 68]. LM-based Joule heating elements are particularly suitable due to their combination of high electrical conductivity, low viscosity, and low vapor pressure. To achieve faster actuation speeds and higher cycling frequencies, it is desirable to increase the current density of Joule heating elements.

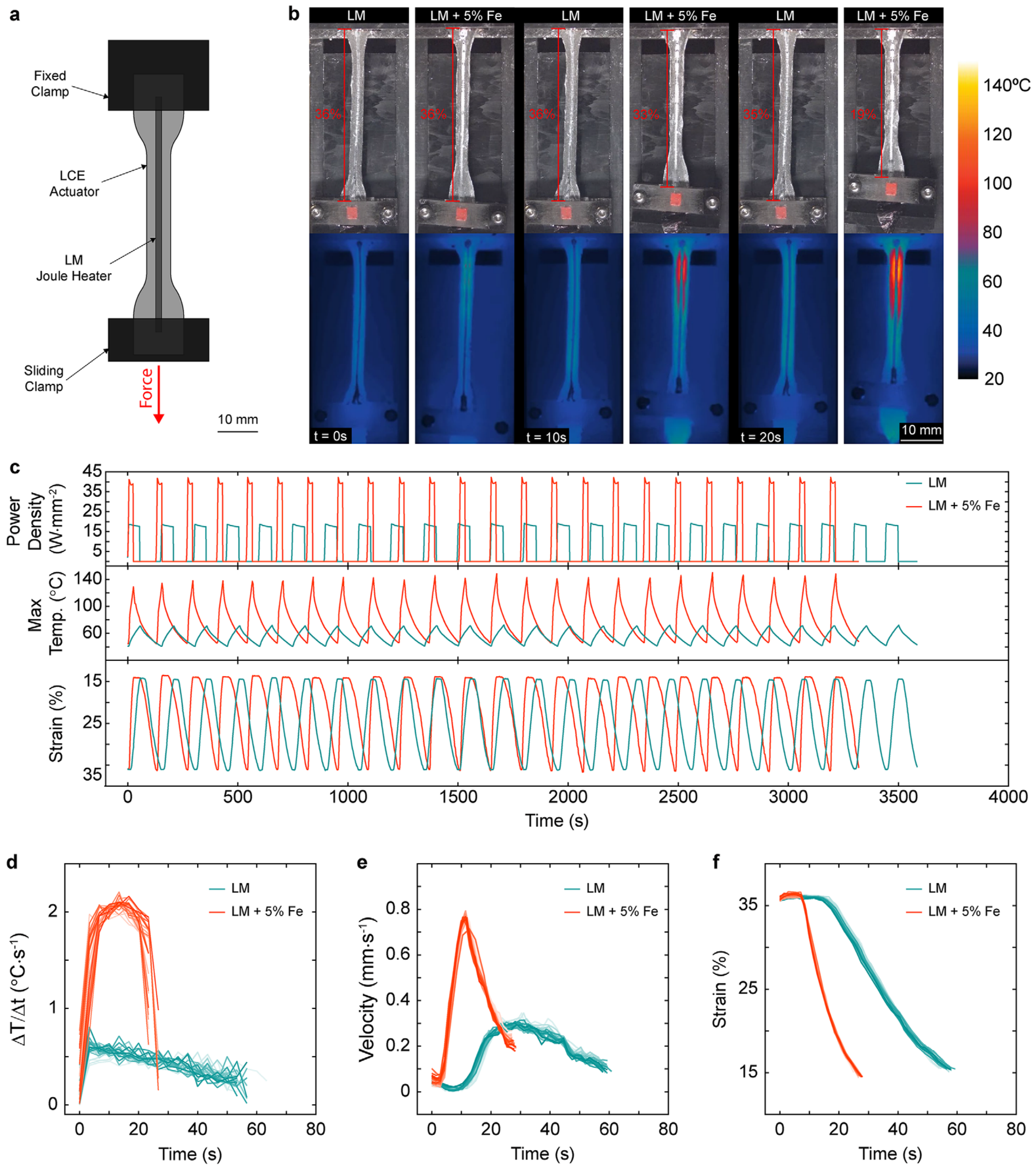

FIGURE 5 | Improved performance of liquid crystal elastomer (LCE) actuators with LM-Fe Joule heating elements. (a) Schematic of LCE actuator with LM-based Joule heating element. (b) Comparison of actuation speed and thermal response of the LCE actuator with pure LM and $\phi = 0.05$ Fe Joule heater over a 20-s span. (c) Comparison of heater power density, maximum LCE actuator temperature, and actuator strain over 24 cycles with a 20% strain stroke length and closed loop control. LCE d) temperature rate, (e) actuator velocity, and (f) actuator strain as a function of time during the heating/retraction phase over 24 cycles for pure LM and $\phi = 0.05$ Fe Joule heaters.

We demonstrate this functionality by creating a closed-loop electrothermal LCE actuator that is activated using an LM-based Joule heating element (Figure 5a; Figure S9). The LCE was loaded with LM (50 vol.%) to improve the thermal conductivity and achieve a more uniform temperature distribution [2]. A LM-based Joule heating element was then patterned on top of the LCE actuator and current was applied using a programmable power supply. An external camera and custom MATLAB script were used to track the position of the actuator and control the output from 15% to 35% strain to lift a 50 g weight (Figure 5b).

To determine the maximum current density of the LM-based Joule heating element, an initial current density of 2×10^7 A·m^{-2} was applied for 24 cycles and increased in increments of 0.25×10^7 A·m^{-2} until the Joule heating element failed. The unfilled LM Joule heater reached a maximum current density of 2.25×10^7 A·m^{-2} without failure (2.5×10^7 A·m^{-2} caused electromigration failure), while the LM-Fe ($\phi = 0.05$) heater operated for 24 cycles at 3×10^7 A·m^{-2}. However, at 3.25×10^7 A·m^{-2}, excessive LCE heating caused vaporization under the Joule heater, destroying the LM trace as the gases escaped.

The LM-Fe Joule heater was able to operate at a higher current density compared to the pure LM Joule heater, leading to higher LCE temperatures and faster actuation over the 20 s actuation period as shown in Figure 5b,c and Movie S2. Specifically, the higher operating current density, coupled with the increased resistivity of the LM-Fe mixture ($\phi = 0.05$), produced a heater power density of approximately 40 $\text{W} \cdot \text{mm}^{-2}$, a 2.2× increase over the unfilled LM heater (Figure 5c). The increased power density resulted in higher maximum temperatures and faster actuation. As observed in the thermal IR imaging in Figure 5b, the LM-Fe heater exhibits localized hot spots during actuation. We interpret that this is a result of geometric thinning and localized resistive heating as the material reaches high strain levels, and not as a loss of electrical continuity. While the conductive path narrows under tension, the presence of solid Fe particles and the growth of a robust Ga-oxide shell provide the structural reinforcement necessary to maintain electrical integrity. This allows the LM-Fe mixture to remain functional at power densities where pure LM would typically cause failure in the heater. The maximum surface temperature of the LCE with the LM-Fe Joule heater reached 150°C, significantly exceeding the 71°C measured with the unfilled LM heater. Consequently, the actuator using the LM-Fe heater completed the 24 cycles nearly 2 cycles faster than the pure LM heater.

To highlight the performance differences between the LM-Fe and pure LM heaters during the heating and cooling phase of the actuation cycle, Figure 5d–f shows the changes in temperature over time, actuator velocity, and strain for both actuators. The average heating rate of the LCE adjacent to the Joule heater was 4× higher at its peak for the LM-Fe heater compared to the pure LM (Figure 5d; Figure S9). Due to the higher heating rate, the LM-Fe actuator was able to achieve a higher maximum velocity (Figure 5e) and strain rate (Figure 5f). Although increasing the maximum current density of the embedded Joule heating element enhanced actuation speed, it is important to note that cycling frequency in electrothermal composites is primarily constrained by heat dissipation to the surrounding environment.

3 | Conclusions

Through this study, we have shown that the addition of relatively small amounts (5% by volume) of metallic particles in LM can greatly enhance the performance and lifespan of stretchable LM interconnects under high current densities with negligible impact on viscosity. We demonstrate that the increase in the maximum current density and time to failure is attributed to the growth of a protective Ga oxide shell, which prevents the formation of voids and hillocks. The protective shell is formed at elevated temperatures and high current densities, a regime where pure LM fails. Although the addition of solid particles slightly reduced the electrical conductivity of the interconnects, the resulting increase in resistive heating and higher Joule heating power density enables electrothermal actuators to achieve faster actuation speeds and higher cyclic frequencies compared to their pure LM counterparts.

Looking forward, integrating these solid particle-LM mixtures into polymer matrices to create LM composites presents a promising path for autonomous soft robotics. While a polymer encapsulation provides elastic recovery and suppresses large-scale LM migration, managing the interfacial adhesion between the LM oxide and the polymer chains will be key to prevent micro-void formation. Our findings here suggest that density-matched fillers are essential in such composites to maintain a robust percolative network under strain. Ultimately, this study on solid particle-LM mixtures advances the knowledge of electromigration mechanism in LM and offers new opportunities for creating more robust LM interconnects for next-generation stretchable electronics and soft robotic systems.

4 | Experimental Section

4.1 | Solid Particle-LM Mixture Fabrication

Gallium and Indium were mixed at 75% Ga and 25% In (Luciteria) by weight to create EGaIn. The filler particles were then mixed into the EGaIn by first hand-mixing the particles to induce EGaIn oxidation and then using a planetary mixer (SpeedMixer DAC 400.2 VAC, FlackTek Inc) to fully incorporate the rigid filler into the EGaIn. The Fe (US5004, 10 μm), and W (US5014, 10 μm) microspheres were purchased from US Research Nanomaterials, and the glass microspheres (440345, 9–13 μm) were purchased from Sigma–Aldrich. The material loading criteria was defined as

$$\left(\phi = \frac{vol(filler)}{vol(filler+LM)}\right).$$

4.2 | Dogbone Sample Fabrication

The dogbone samples were created by first laser-cutting the dogbone shape into a laser mask (Blazer Orange Laser Mask, Ikonics Imaging). The mask was then adhered to a high-temperature quartz sheet (7784N13, McMaster-Carr). A thin layer of LM was airbrushed onto the sheet to increase wetting between the quartz and LM mixture. The LM mixture was then applied by blade-coating with a silicone spatula. The orange laser mask was removed, leaving the dogbone shape of the LM mixture. Before testing, the profile of the sample was measured using a profilometer (VK-X200K; Keyence) to estimate the average cross-sectional area at the center of the dogbone sample. All samples were manually adjusted to an average cross-sectional area of 0.143 ± 0.011 mm^2 to ensure consistent results. After measuring the cross-section, the samples were placed in a furnace set to the prescribed temperature (150–900°C) for 30 min. After the samples were removed and cooled, the cross-section was again measured to ensure it remained similar.

4.3 | Failure Current Characterization

The cross-section of each sample was measured using a laser scanning microscope. A 2.4 mm diameter W electrode was placed on each sample contact pad prior to laser scanning to account for any change in cross-section due to displacement of the LM caused by the electrodes used in electrical testing. The samples were adhered with thermal paste to a stainless steel optical table to help dissipate the heat generated by Joule heating. The tungsten electrodes were placed on the contact pads of the sample and were connected to a DC power source (2260B, Keithley). A current of 0.5 A was applied to the sample for 30 s and the current was increased by 0.5 A every 30 s until open-circuit electrical failure of the dogbone sample occurred.

4.4 | Conductivity Measurements

The LM mixture was injected into a section of clear polyethylene tubing with an internal diameter of 4.26 mm. Copper electrodes of the same diameter were inserted into the ends of the tubing to seal in the LM. The distance between the copper electrodes was 150 mm. A source meter (2461; Keithley) with a four-wire setup was attached to the copper electrodes and a 100 mA current (I) was applied across the sample. Five voltage (V) measurements were recorded over a 30 s period using a custom MATLAB script. The electrical conductivity $\sigma = \frac{I\,L}{V\,A}$ was calculated, where A and L are the area and length of the LM conductor.

4.5 | Viscosity Measurements

The viscosity of solid particle-LM mixtures was measured using a rheometer (AR1500ex; TA Instruments) with an 8 mm diameter parallel plate geometry at ambient conditions (20°C) over a shear rate range of $\dot{\gamma} = 10^{-2} - 10^{2}\ s^{-1}$. To ensure an adequate amount of filler materials was included in the sample for each viscosity measurement, a gap height of 1 mm was used. Immediately before loading the sample onto the rheometer stage, the sample was stirred to ensure the tested sample was homogeneous. After lowering the geometry to the 1 mm gap height, the geometry was rotated at 0.5 $\text{rad} \cdot \text{s}^{-1}$ to spread out the sample. The excess LM-particle mixture was then removed. For each sample, the measurement was repeated three times ($n = 3$). A new LM-particle mixture sample was used for each test.

4.6 | Time-to-Failure Measurements

Dogbone samples were fabricated and the cross-sections were measured using the methods described in the Failure Current Characterization section. The constant current required to achieve the desired current density was then calculated using the sample cross-section. A constant current was applied using a DC power source (2260B, Keithley) until open-circuit failure. Voltage data was continuously recorded with a Raspberry Pi and custom Python script over the duration of the test.

4.7 | Joule Heater Demonstration

The actuator mold was machined from an HDPE sheet using a three-axis desktop CNC mill (Bantam Tools). The LCE with LM inclusions was synthesized using previously described methods [13, 69]. The Joule heater was applied to the LCE actuator by blade coating. The cross-section of the Joule heater was measured with the laser scanning microscope, and the required current for each tested current density was calculated. The LCE actuator was attached horizontally to two acetal clamps atop an acetal surface, as shown in the schematic in Figure S9c. A 50 g mass was applied to the actuator and the actuator was pre-strained for three cycles before testing. A camera and custom MATLAB script controlled the output of the power supply based on the measured strain and recorded a video of the experiment. An infrared camera (A700; FLIR) recorded temperature data.

Acknowledgments

The authors acknowledge support through the National Science Foundation (Nos. CMMI-2339780, EEC-2050587), NASA Nebraska EPSCoR (80NSSC19M0065), and the Nebraska Tobacco Settlement Biomedical Research Development Fund. Manufacturing and characterization analysis were performed at the NanoEngineering Research Core Facility, National Nanotechnology Coordinated Infrastructure, and the Nebraska Center for Materials and Nanoscience, which are supported by the National Science Foundation under Award ECCS: 1542182, and the Nebraska Research Initiative.

Conflicts of Interest

The authors declare no conflicts of interest.

Data Availability Statement

The data that support the findings of this study are available from the corresponding author upon reasonable request.

References

1. C. J. Thrasher, Z. J. Farrell, N. J. Morris, C. L. Willey, and C. E. Tabor, "Mechanoresponsive Polymerized Liquid Metal Networks," *Advanced Materials* 31, no. 40 (2019): 1903864.

2. M. J. Ford, C. P. Ambulo, T. A. Kent, et al., "A Multifunctional Shape-Morphing Elastomer with Liquid Metal Inclusions," *Proceedings of the National Academy of Sciences of the United States of America* 116, no. 43 (2019): 21438–21444.

3. T. P. Chenal, J. C. Case, J. Paik, and R. K. Kramer, "Variable Stiffness Fabrics with Embedded Shape Memory Materials for Wearable Applications," in *2014 IEEE/RSJ International Conference on Intelligent Robots and Systems* (IEEE, 2014), 2827–2831.

4. G. Mao, M. Drack, M. Karami-Mosammam, et al., "Soft Electromagnetic Actuators," *Science Advances* 6, no. 26 (2020): eabc0251.

5. T. N. Do, H. Phan, T.-Q. Nguyen, and Y. Visell, "Miniature Soft Electromagnetic Actuators for Robotic Applications," *Advanced Functional Materials* 28, no. 18 (2018): 1800244.

6. R. Guo, L. Sheng, H. Gong, and J. Liu, "Liquid Metal Spiral Coil Enabled Soft Electromagnetic Actuator," *Science China Technological Sciences* 61, no. 4 (2018): 516–521.

7. E. J. Barron III, R. S. Peterson, N. Lazarus, and M. D. Bartlett, "Mechanically Cloaked Multiphase Magnetic Elastomer Soft Composites for Wearable Wireless Power Transfer," *ACS Applied Materials & Interfaces* 12, no. 45 (2020): 50909–50917.

8. L. Han, J. Si, M. Guo, et al., "An Untethered Soft Crawling Robot Driven by Wireless Power Transfer Technology," *Small* 20, no. 27 (2024): 2309661.

9. A. R. P. Mathai, T. Stalin, and P. V. y Alvarado, "Flexible Fiber Inductive Coils for Soft Robots and Wearable Devices," *IEEE Robotics and Automation Letters* 7, no. 2 (2022): 5711–5718.

10. M. D. Dickey, R. C. Chiechi, R. J. Larsen, E. A. Weiss, D. A. Weitz, and G. M. Whitesides, "Eutectic Gallium–Indium (EGaIn): A Liquid Metal Alloy for the Formation of Stable Structures in Microchannels at Room Temperature," *Advanced Functional Materials* 18, no. 7 (2008): 1097–1104.

11. R. C. Chiechi, E. A. Weiss, M. D. Dickey, and G. M. Whitesides, "Eutectic Gallium–Indium (EGaIn): A Moldable Liquid Metal for Electri-

cal Characterization of Self-Assembled Monolayers," *Angewandte Chemie International Edition* 47, no. 1 (2008): 142–144.

12. T. Liu, P. Sen, and C.-J. Kim, "Characterization of Nontoxic Liquid-Metal Alloy Galinstan for Applications in Microdevices," *Journal of Microelectromechanical Systems* 21, no. 2 (2012): 443–450.

13. T. A. Kent, M. J. Ford, E. J. Markvicka, and C. Majidi, "Soft Actuators Using Liquid Crystal Elastomers with Encapsulated Liquid Metal Joule Heaters," *Multifunctional Materials* 3, no. 2 (2020): 025003.

14. K. L. Dorsey and N. Lazarus, "Lifetime of Liquid Metal Wires for Stretchable Devices," *Advanced Materials Technologies* 6, no. 4 (2021): 2001100.

15. H. O. Michaud and S. P. Lacour, "Liquid Electromigration in Gallium-Based Biphasic Thin Films,"*APL Materials* 7, no. 3 (2019).

16. Y.-G. Park, H. Min, H. Kim, A. Zhexembekova, C. Y. Lee, and J.-U. Park, "Three-Dimensional, High-Resolution Printing of Carbon Nanotube/Liquid Metal Composites with Mechanical and Electrical Reinforcement," *Nano Letters* 19, no. 8 (2019): 4866–4872.

17. M. D. Bartlett, A. Fassler, N. Kazem, E. J. Markvicka, P. Mandal, and C. Majidi, "Stretchable, High-k Dielectric Elastomers through Liquid-Metal Inclusions," *Advanced Materials* 28, no. 19 (2016): 3726–3731.

18. S. Liu, D. S. Shah, and R. Kramer-Bottiglio, "Highly Stretchable Multilayer Electronic Circuits Using Biphasic Gallium-Indium," *Nature Materials* 20, no. 6 (2021): 851–858.

19. E. J. Markvicka, M. D. Bartlett, X. Huang, and C. Majidi, "An Autonomously Electrically Self-Healing Liquid Metal–Elastomer Composite for Robust Soft-Matter Robotics and Electronics," *Nature Materials* 17, no. 7 (2018): 618–624.

20. C. Pan, E. J. Markvicka, M. H. Malakooti, et al., "A Liquid-Metal–Elastomer Nanocomposite for Stretchable Dielectric Materials," *Advanced Materials* 31, no. 23 (2019): 1900663.

21. F. Krisnadi, T. Sakorikar, M. H. Vong, and M. D. Dickey, "Improved Direct Ink Writing of Liquid Metal Foams via Liquid Additives," *Advanced Electronic Materials* (2025): 2500009.

22. S. J. Woodman, D. S. Shah, M. Landesberg, A. Agrawala, and R. Kramer-Bottiglio, "Stretchable Arduinos Embedded in Soft Robots," *Science Robotics* 9, no. 94 (2024): eadn6844.

23. E. J. Krings, H. Zhang, S. Sarin, J. E. Shield, S. Ryu, and E. J. Markvicka, "Lightweight, Thermally Conductive Liquid Metal Elastomer Composite with Independently Controllable Thermal Conductivity and Density," *Small* 17, no. 52 (2021): 2104762.

24. M. D. Bartlett, N. Kazem, M. J. Powell-Palm, et al., "High Thermal Conductivity in Soft Elastomers with Elongated Liquid Metal Inclusions," *Proceedings of the National Academy of Sciences of the United States of America* 114, no. 9 (2017): 2143–2148.

25. R. Tutika, S. H. Zhou, R. E. Napolitano, and M. D. Bartlett, "Mechanical and Functional Tradeoffs in Multiphase Liquid Metal, Solid Particle Soft Composites," *Advanced Functional Materials* 28, no. 45 (2018): 1804336.

26. Y. Han, S. S. Rohewal, S. Gupta, S. Paul, C. C. Bowland, and M. H. Malakooti, "Conductive Liquid Metal Vitrimer Composites for Reconfigurable and Recyclable Flexible Electronics," *Advanced Functional Materials* 35, no. 50 (2025): e11119.

27. Y. Han, H. Tetik, and M. H. Malakooti, "3D Soft Architectures for Stretchable Thermoelectric Wearables with Electrical Self-Healing and Damage Tolerance," *Advanced Materials* 36, no. 49 (2024): 2407073.

28. J. R. Black, "Electromigration–A Brief Survey and Some Recent Results," *IEEE Transactions on Electron Devices* 16, no. 4 (1969): 338–347.

29. P. Kumar, "Chapter 5 – Electromigration in Metallic Materials and Its Role in Whiskering," in *Handbook of Solid State Diffusion*, A. Paul and S. Divinski, Eds., Vol. 2 (Elsevier, 2017), 173–206.

30. R. Ma, C. Guo, Y. Zhou, and J. Liu, "Electromigration Induced Break-up Phenomena in Liquid Metal Printed Thin Films," *Journal of Electronic Materials* 43, no. 11 (2014): 4255–4261.

31. D. Stroud, "Calculations of the Average Driving Force for Electromigration in Liquid-Metal Alloys," *Physical Review B* 13 (1976): 4221–4226.

32. S. Kumar, P. Kumar, and R. Pratap, "A Model for Electromigration Induced Flow in Liquid Metals," *Journal of Physics D: Applied Physics* 50, no. 39 (2017): 39LT02.

33. I. Dutta and P. Kumar, "Electric Current Induced Liquid Metal Flow: Application to Coating of Micropatterned Structures," *Applied Physics Letters* 94, no. 18 (2009): 184104.

34. R. Sorbello, "Electromigration in Liquid Metal Alloys," *Physica Status Solidi B* 86, no. 2 (1978): 671–678.

35. A. Hirsch and S. P. Lacour, "A Method to Form Smooth Films of Liquid Metal Supported by Elastomeric Substrate," *Advanced Science* 5, no. 10 (2018): 1800256.

36. P. Kumar, J. Howarth, and I. Dutta, "Electric Current Induced Flow of Liquid Metals: Mechanism and Substrate-Surface Effects," *Journal of Applied Physics* 115, no. 4 (2014): 44915.

37. W. Kong, Z. Wang, M. Wang, et al., "Oxide-Mediated Formation of Chemically Stable Tungsten– Liquid Metal Mixtures for Enhanced Thermal Interfaces," *Advanced Materials* 31, no. 44 (2019): 1–8.

38. W. Kong, Z. Wang, N. Casey, et al., "High Thermal Conductivity in Multiphase Liquid Metal and Silicon Carbide Soft Composites," *Advanced Materials Interfaces* 8, no. 14 (2021): 2100069.

39. J. Tang, X. Zhao, J. Li, R. Guo, Y. Zhou, and J. Liu, "Gallium-Based Liquid Metal Amalgams: Transitional-State Metallic Mixtures (Transm^{2}ixes) with Enhanced and Tunable Electrical, Thermal, and Mechanical Properties," *ACS Applied Materials & Interfaces* 9, no. 41 (2017): 35977–35987.

40. M. I. Ralphs, N. Kemme, P. B. Vartak, et al., "In Situ Alloying of Thermally Conductive Polymer Composites by Combining Liquid and Solid Metal Microadditives," *ACS Applied Materials & Interfaces* 10, no. 2 (2018): 2083–2092.

41. C. Cho, W. Shin, M. Kim, et al., "Monolithically Programmed Stretchable Conductor by Laser-Induced Entanglement of Liquid Metal and Metallic Nanowire Backbone," *Small* 18, no. 37 (2022): 2202841.

42. M. Kim, C. Cho, W. Shin, et al., "Nanowire-Assisted Freestanding Liquid Metal Thin-Film Patterns for Highly Stretchable Electrodes on 3D Surfaces," *npj Flexible Electronics* 6, no. 1 (2022): 1–8.

43. S. Eristoff, A. M. Nasab, X. Huang, and R. Kramer-Bottiglio, "Liquid Metal + X: A Review of Multiphase Composites Containing Liquid Metal and Other (X) Fillers," *Advanced Functional Materials* 34, no. 31 (2024): 2309529.

44. A. Hajalilou, A. F. Silva, P. A. Lopes, E. Parvini, C. Majidi, and M. Tavakoli, "Biphasic Liquid Metal Composites for Sinter-Free Printed Stretchable Electronics," *Advanced Materials Interfaces* 9, no. 5 (2022): 2101913.

45. A. Hajalilou, E. Parvini, J. P. M. Pereira, et al., "Digitally Printable Magnetic Liquid Metal Composite for Recyclable Soft-Matter Electronics," *Advanced Materials Technologies* 8, no. 10 (2023): 2201621.

46. M. Reis Carneiro, C. Majidi, and M. Tavakoli, "Gallium-Based Liquid–Solid Biphasic Conductors for Soft Electronics," *Advanced Functional Materials* 33, no. 41 (2023): 2306453.

47. B. Yuan, C. Zhao, X. Sun, and J. Liu, "Lightweight Liquid Metal Entity," *Advanced Functional Materials* 30, no. 14 (2020): 1910709.

48. Z. Luo and X.-P. Zhou, "Liquid Metal–Induced Low-Temperature Synthesis of Tunable High-Entropy Oxides," *Science Advances* 11, no. 23 (2025): eadw1461.

49. Z. Luo and X.-P. Zhou, "Liquid-Metal-Mediated Low-Temperature Sintering Synthesis of High-Entropy Alloys with On-Demand Composition and Performance,"*Cell Reports Physical Science* 6, no. 12 (2025).

50. Z. Luo and X.-P. Zhou, "Liquid Metal Chemical Plating Rheological Modification Method for Magnetic Metal Materials," *Advanced Functional Materials* 35, no. 9 (2025): 2416231.

51. J. Hu and X.-P. Zhou, "MXene/Liquid Metal Electrospinning Film for High-Performance Strain Sensors," *ACS Applied Nano Materials* 9, no. 11 (2026): 5156–5164.

52. X.-P. Zhou, Z. Luo, and D.-X. Yang, "Liquid Metal Hydrothermal Rheological Modification Method for High Performance Gallium-Coated Carbon Microparticle Composites," *Advanced Materials Technologies* 10, no. 2 (2025): 2400737.

53. C. Wang, Y. Gong, B. V. Cunning, et al., "A General Approach to Composites Containing Nonmetallic Fillers and Liquid Gallium," *Science Advances* 7, no. 1 (2021): eabe3767.

54. W. Kong, Z. Wang, M. Wang, et al., "Oxide-Mediated Formation of Chemically Stable Tungsten– Liquid Metal Mixtures for Enhanced Thermal Interfaces," *Advanced Materials* 31, no. 44 (2019): 1904309.

55. M. D. Dickey, R. C. Chiechi, R. J. Larsen, E. A. Weiss, D. A. Weitz, and G. M. Whitesides, "Eutectic Gallium-Indium (EGaIn): A Liquid Metal Alloy for the Formation of Stable Structures in Microchannels at Room Temperature," *Advanced Functional Materials* 18, no. 7 (2008): 1097–1104.

56. S. Yu and M. Kaviany, "Electrical, Thermal, and Species Transport Properties of Liquid Eutectic Ga–In and Ga–In–Sn from First Principles," *The Journal of Chemical Physics* 140, no. 6 (2014): 064303.

57. D. Zrnic and D. S. Swatik, "On the Resistivity and Surface Tension of the Eutectic Alloy of Gallium and Indium," *Journal of the Less Common Metals* 18, no. 1 (1969): 67–68.

58. W. Kong, N. U. H. Shah, T. V. Neumann, et al., "Oxide-Mediated Mechanisms of Gallium Foam Generation and Stabilization During Shear Mixing in Air," *Soft Matter* 16, no. 25 (2020): 5801–5805.

59. F. Krisnadi, S. Kim, S. Im, et al., "Printable Liquid Metal Foams That Grow When Watered," *Advanced Materials* 36, no. 34 (2024): 2308862.

60. S. Liu, S. N. Reed, M. J. Higgins, M. S. Titus, and R. Kramer-Bottiglio, "Oxide Rupture-Induced Conductivity in Liquid Metal Nanoparticles by Laser and Thermal Sintering," *Nanoscale* 11 (2019): 17615–17629.

61. J. Cutinho, B. S. Chang, S. Oyola-Reynoso, et al., "Autonomous Thermal-Oxidative Composition Inversion and Texture Tuning of Liquid Metal Surfaces," *ACS Nano* 12, no. 5 (2018): 4744–4753.

62. Y. Jeong, O. Douglas, U. Misra, et al., "Mitigation of Electromigration in Metal Interconnects via Hexagonal Boron Nitride as an Ångström-Thin Passivation Layer," *Advanced Electronic Materials* 7, no. 6 (2021): 2100002.

63. J. Koster, "Directional Solidification and Melting of Eutectic GaIn," *Crystal Research and Technology* 34, no. 9 (1999): 1129–1140.

64. Y. Lin, J. Genzer, and M. D. Dickey, "Attributes, Fabrication, and Applications of Gallium-Based Liquid Metal Particles," *Advanced Science* 7, no. 12 (2020): 2000192.

65. S. I. Rich, R. J. Wood, and C. Majidi, "Untethered Soft Robotics," *Nature Electronics* 1, no. 2 (2018): 102–112.

66. A. Miriyev, K. Stack, and H. Lipson, "Soft Material for Soft Actuators," *Nature Communications* 8, no. 1 (2017): 596.

67. C. Yuan, D. J. Roach, C. K. Dunn, et al., "3D-Printed Reversible Shape-Changing Soft Actuators Assisted by Liquid Crystal Elastomers," *Soft Matter* 13, no. 33 (2017): 5558–5568.

68. J. D. Carrico, K. J. Kim, and K. K. Leang, "3D-Printed Ionic Polymer-Metal Composite Soft Crawling Robot," in *2017 IEEE International Conference on Robotics and Automation* (IEEE, 2017), 4313–4320.

69. M. O. Saed, A. H. Torbati, D. P. Nair, and C. M. Yakacki, "Synthesis of Programmable Main-Chain Liquid-Crystalline Elastomers Using a Two-Stage Thiol-Acrylate Reaction," *Journal of Visualized Experiments* 1, no. 107 (2016): e53546.

Supporting Information

Additional supporting information can be found online in the Supporting Information section.

Supporting File 1: admt71060-sup-0001-SuppMat.pdf.
Supporting File 2: admt71060-sup-0002-MovieS1.mp4.
Supporting File 3: admt71060-sup-0003-MovieS2.mp4.